Nonlinear Focal Modulation Microscopy

Guangyuan Zhao,[1,*] Cheng Zheng,[1,*] Cuifang Kuang,[1,5,†] Renjie Zhou,[2] Mohammad M. Kabir,[3] Kimani C. Toussaint, Jr.,[4] Wensheng Wang,[1] Liang Xu,[1] Haifeng Li,[1] Peng Xiu,[1] and Xu Liu[1,5,‡]

[1]*State Key Laboratory of Modern Optical Instrumentation, College of Optical Science and Engineering, Zhejiang University, Hangzhou, Zhejiang 310027, China*

[2]*Department of Biomedical Engineering, The Chinese University of Hong Kong, Shatin, New Territories, Hong Kong, China*

[3]*Department of Electrical and Computer Engineering, University of Illinois Urbana-Champaign, Urbana, Illinois 61801, USA*

[4]*Department of Mechanical Science and Engineering, University of Illinois Urbana-Champaign, Urbana, Illinois 61801, USA*

[5]*Collaborative Innovation Center of Extreme Optics, Shanxi University, Taiyuan 030006, China*

(Received 30 October 2017; published 9 May 2018)

We demonstrate nonlinear focal modulation microscopy (NFOMM) to achieve superresolution imaging. Traditional approaches to superresolution that utilize point scanning often rely on spatially reducing the size of the emission pattern by directly narrowing (e.g., through minimizing the detection pinhole in Airyscan, Zeiss) or indirectly peeling its outer profiles [e.g., through depleting the outer emission region in stimulated emission depletion (STED) microscopy]. We show that an alternative conceptualization that focuses on maximizing the optical system's frequency shifting ability offers advantages in further improving resolution while reducing system complexity. In NFOMM, a spatial light modulator and a suitably intense laser illumination are used to implement nonlinear focal-field modulation to achieve a transverse spatial resolution of ~60 nm ($\sim\lambda/10$). We show that NFOMM is comparable with STED microscopy and suitable for fundamental biology studies, as evidenced in imaging nuclear pore complexes, tubulin and vimentin in Vero cells. Since NFOMM is readily implemented as an add-on module to a laser-scanning microscope, we anticipate wide utility of this new imaging technique.

DOI: 10.1103/PhysRevLett.120.193901

In the past two decades, a number of coordinate-targeted superresolution methods [1,2] have been demonstrated that modulate fluorescence emission patterns by manipulating the illumination beam [3–7]. The corresponding illumination patterns can be categorized as either structured illumination (SI) or point illumination (PI), where the former is widely implemented in structured illumination microscopy (SIM) [8,9] and the latter in confocal microscopy [10]. In order to surpass the twofold enhancement in spatial resolution that comes with these techniques, it is necessary to introduce nonlinearity in the excitation-emission process by utilizing a high illumination density, as is the case with both stimulated emission depletion (STED) microscopy [3] and saturated structured illumination microscopy (SSIM) [11,12]. In the case of STED, its widespread adoption suggests that PI is a better choice to implement saturation techniques since it can easily offer a high illumination density through strong focusing, as well as deep tissue imaging [13] through the use of a pinhole [14]. While STED avoids the large number of recordings required in SSIM, it still suffers from potential unwanted reexcitation arising from the infrared illumination and high-power depletion beam [15–18]. Moreover, both SSIM and STED require relatively complex experimental platforms. Recently, several groups have implemented SIM-based algorithms for postprocessing in imaging scanning microscopy (ISM) [19–21], a modification of confocal microscopy, to obtain extraordinary efficacy of resolution enhancement using either linear [22,23] or saturation [24] processes. However, the use of a Gaussian input beam still results in an emission pattern with few high-frequency components, prohibiting substantial improvement of resolution under fluorescence saturation.

In this Letter, we overcome the aforementioned issues by finding a feasible and flexible scheme that incorporates many of the advantages of confocal microscopy while surpassing the twofold enhancement in spatial resolution. Note that all reported PI-based superresolution methods employ the mechanism of minimizing the spatial extent of the fluorescence emission point spread function (PSF) [19,25–31]. Along this line, we have previously introduced fluorescence emission difference microscopy, which utilizes the subtraction of two recordings in postprocessing, one from a doughnut beam and the other from a Gaussian beam, in order to simplify the complexity of the experimental platform. However, the resolution is limited to $\lambda/6$, and the result suffers unpleasant negative values due to the mismatch of the two recordings' profiles. It is also worth noting that, while the use of a doughnut illumination beam has been routinely employed to obtain superresolution [32,33], these approaches have focused on minimizing the center of the doughnut spot, i.e., obtaining a spatially

reduced on-axis intensity null. However, this conceptualization obscures behavior in the spatial-frequency domain via the optical transfer function, namely, that there remains an absence in critical spatial frequencies for imaging continuous biological samples. It therefore becomes instructive to consider the frequency shifting mechanism [2] conceptualization, where we learn that superresolution can be achieved by maximizing the overall coverage of emission patterns in the Fourier domain.

Thus, in this Letter, we emphasize the frequency shifting concept as a general basis in the PI-based imaging approaches and introduce nonlinear focal modulation microscopy (NFOMM) as a technique that uses high-intensity modulated-pattern scanning. In NFOMM, through judicious focal light-field modulations, namely, frequency reassigned illumination PSF through phase modulation and saturated excitation modulation through intense illumination, prominent high-frequency components from the target object are retained in the nonlinear emission. After shifting the object's high spatial resolution information into the system's detection passband under one or multiple phase modulations, we postprocess acquired recordings using a forward model described by the effective system optical transfer functions ($\mathrm{OTF_{eff}}$) to reconstruct the superresolved object.

Principle.—Shown in Fig. 1(a), the illumination pattern of a PI microscope is formed under vectorial diffraction theory [34,35]. Using a desired polarization and encoded phase delay, the incident light is focused by an objective lens and generates an illumination pattern onto the sample plane [Fig. 1(a) (I–II)]. In a classical PI microscope, assuming a linear photon-response and no phase modulation [Fig. 1(b) (I)], the sample's emitted fluorescence yields a Gaussian PSF [Fig. 1(b) (IV)]. Herein we examine two illumination patterns, doughnut and line-shape, generated by modulating the phase of incident beam with the masks shown in Fig. 1(b) (II–III). When increasing the intensity of the two phase-modulated illuminations, the emission patterns from the sample are nonlinearly modulated by both the doughnut or line shape illumination and the fluorescence saturation [Fig. 1(a) (III)]. The corresponding $\mathrm{OTF_{eff}}$ of the above three emission patterns are shown in the third row of Fig. 1(b), where the saturated doughnut emission (SDE) yields stronger high-frequency components and the y direction saturated line shape emission (SLE) covers more high-frequency components than the previous two emission patterns along the x direction. Figure 1(c) gives the normalized x direction line profiles of the $\mathrm{OTF_{eff}}$ to intuitively compare the performances between three different emission patterns. When increasing the illumination intensity to 100 $\mathrm{kW/cm^2}$, the nonlinear effect due to fluorescence saturation extends the $\mathrm{OTF_{eff}}$ of saturated Gaussian emission (GE) to be beyond that of the nonsaturated counterpart. The SDE pattern, as well as the SLE pattern, expands the frequency band, and importantly, their

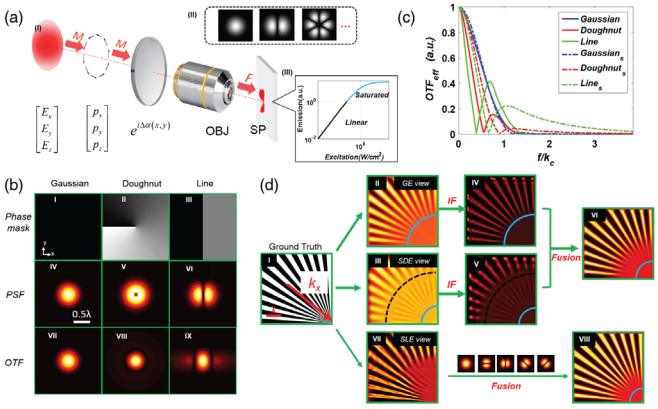

FIG. 1. Working principle. (a) Sketch of focal modulation. (I) The illuminated wave front $[E_x, E_y, E_z]$ is modulated, by multiplying (M) the phase delay $e^{i\Delta\alpha(x,y)}$ with the polarization $[p_x, p_y, p_z]$, and then focused by an objective (OBJ) onto the sample plane (SP). (II) Example PSFs. (III) Fluorescent saturation curve simulated using rhodamine 6G [37]. (b) (I–III) Zero, $0-2\pi$ vortex, and $0-\pi$ step phase masks; (IV-VI) and (VII-IX) are the resulting $\mathrm{PSF_{eff}}$ and $\mathrm{OTF_{eff}}$. The emitted Gaussian PSF is nonsaturated, while that for the doughnut and line shape PSFs are all saturated. The size of the detection pinhole is assumed to be 0.6 A.U. diameter. (c) Normalized profiles of the $\mathrm{OTF_{eff}}$ corresponding to nonsaturated Gaussian (blue line), doughnut (red line), and line shape (green line) emission patterns and their counterparts (dashed lines) under saturated condition. (d) Imaging results of the spokelike sample [indicated in (d), (I)] with nonsaturated GE [indicated in (d) (II)] and SDE [indicated in (d) (III)], respectively. (d) (IV and V) Recovered RL deconvolution results of (d) (II and III), respectively; (d) (VI) is the NFOMM result from (d) (II and III) with multiview reconstruction. (d) (I) The recovered result of a single SLE image; (d) (II) is the NFOMM result reconstructed from the multiview reconstruction, using recordings generated by the SLE patterns with four orientations and a GE pattern. Here, k_x in (d) (I) denotes the direction of the object's spatial-frequency increase. The light blue circles (d) denote the borders beyond which one can barely discern object details, and the related spatial-frequency component will be cut off. The black dashed circles (d) denote the frequency deficiency regions. Herein, "nonsaturated" corresponds to a peak illumination intensity of 3 $\mathrm{kW/cm^2}$, while the saturated corresponds to a peak illumination intensity of 100 $\mathrm{kW/cm^2}$. Iterations (d) are all 200.

high-frequency components increase drastically in comparison to the saturated GE pattern. Therefore, the SDE and SLE give a wider $\mathrm{OTF_{eff}}$ distribution, thereby leading to a better spatial resolution. Notably, the lack of high-frequency components in $\mathrm{OTF_{eff}}$ with saturated GE pattern explains why the experimental resolution enhancement of point-scanning saturated SIM is limited to 2.6 folds [24]. This also explains why the resolution of saturated GE-based saturated excitation microscopy (SAX) has not yet achieved a resolution beyond 140 nm (for 532-nm excitation wavelength) [36].

The SDE and SLE patterns shift the sample's high-frequency components into the passband of the OTF_{det}. Next, a postprocessing algorithm is essential for deconvolving the raw data to obtain the final superresolved image. The reconstruction is considered as an inverse problem, i.e., an estimation of the original sample structure using the system's forward model and recordings. To efficiently reconstruct information, we apply a positively constrained single-view or multiview Richardson-Lucy (RL) reconstruction algorithm with the forward model (see details about reconstruction and the forward model in the Supplemental Material, Sec. II [38]).

A spokelike sample [Fig. 1(d) (I)], is simulated to verify NFOMM's frequency retaining ability. We begin with a comparison between the performance of GE in Fig. 1(d) (II) and the SDE in Fig. 1(d) (III). We find that the circle diameter in the latter is much smaller than that in the former [Fig. 1(d) (III)], indicating a higher achievable resolution. However, the dual crests feature of the doughnut emission PSF induces inner-region malposition in Fig. 1(d) (III), reflecting a contrast inversion in the complex amplitude. In Figs. 1(d) (IV and V), inverse filtering (IF) makes the already recognized regions more distinct and the reconstructed spokes thinner [52]. Apparently, NFOMM achieves subtler details without the malpositioning issue, confirming the strength of the technique.

NFOMM has the flexibility to incorporate multiple recordings acquired under different modulation conditions to render a superior result. Note that in NFOMM the retrieved sample frequency with a single-view SDE recording suffers deficiency at a certain point [corresponding to the valley of the dashed red line in Fig. 1(c)], where the frequency strength is orders of magnitude lower than its neighborhoods. Indicated by the black dashed circles in Fig. 1(d) (III and V), the frequency deficiency from SDE renders blurred regions. The deficiency does not severely influence the reconstructed results in imaging the discrete fluorescent nanoparticles with this SDE-based single-view (referring to retrieving with only a single recording, which in this case is a doughnut recording) NFOMM, but is detrimental in imaging continuous samples such as the microtubules. However, by utilizing multiview fusion, we combine the advantages of the two illuminations through superposing the Fourier spectrums of the GE recording with that of SDE recording to obtain a synthetized Fourier spectrum, termed dual-view NFOMM; i.e., the GE and SDE recordings are regarded as two views. Figure 1(d) (VI) shows an instance of this dual-view NFOMM result, where the once annular blurred region has now been compensated and image blurring is further decreased.

To further verify NFOMM's capacity, we examine NFOMM's performance with the SLE modulation. Shown in Fig. 1(d) (VII), the recovered result from a single y direction SLE recording [Fig. 1(b) (VI)] achieves a better resolution along the x direction due to the abundant high-frequency components in this direction. However, lacking the y direction frequency components, the spokes are blurred and distorted along the clockwise direction. Therefore, we make four SLE recordings with four illumination orientations (0°, 45°, 90°, and 135° relative to the x direction) and one GE recording for a multiview NFOMM fusion. The corresponding SLE-based multiview NFOMM result [Fig. 1(d) (VIII)] achieves improved resolution in all directions without blurring. Considering that the SLE-NFOMM demands multiple recordings and is more vulnerable to photobleaching and aberrations, this Letter mainly evaluates NFOMM's experimental performance with the SDE modulation mode.

Examining the resolution of single-view NFOMM.— We conduct a series of experiments utilizing our NFOMM system, detailed in the Supplemental Material, Sec. I [38]. First, we image fluorescent nanoparticles [F8789-FluoSphere carboxylate-modified microspheres, 0.04 μm, dark red (660,680)] with a continuous-wave laser source at an illumination wavelength of 635 nm and a pinhole size of 0.74 a.u. Our results [Fig. 2(b)] show a significant resolution improvement compared to those obtained using standard confocal microscopy [Fig. 2(a)]. We can observe in the confocal images an apparent aggregation of nanoparticles, which are clearly resolved to reveal discrete nanoparticles in the NFOMM images. Also, density profiles along the green dashed lines in Figs. 2(a) and 2(b) show a discernible distance of 93 nm ($\sim\lambda/7$) between two adjacent nanoparticles with an illumination power of 90 μW. Nanoparticles that once appeared as one (in the magenta confocal curve) now appear as two separated peaks (in the green NFOMM curve) in Fig. 2(c). Additional details are shown in the Supplemental Material, Fig. S5 [38], where we also include a comparison between NFOMM and deconvolved confocal.

Since the signal at the detector is the saturated emission fluorescence from the stained sample, the signal level of NFOMM is 4–10 folds larger than confocal. However, a

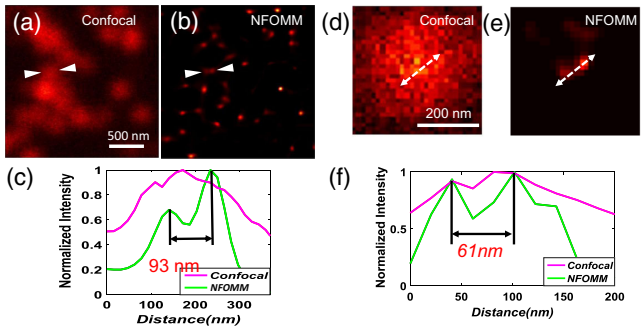

FIG. 2. (a),(b) NFOMM results of 40 nm fluorescent nanoparticles with a pinhole size of 0.74 A.U. (c) Density profiles along the green dashed lines in (a),(b) show a resolution of $\lambda/7$. (d),(e) NFOMM applied with a pinhole size narrowed to 0.37 A.U. (f) Density profiles along the white dashed lines in (d),(e) verifies a resolution of $\lambda/10$.

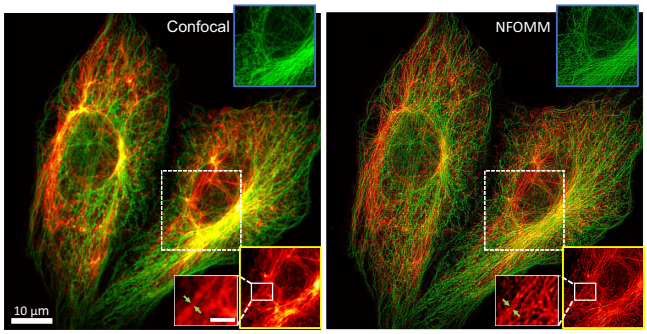

FIG. 3. Dual-color NFOMM applied to Vero cells in comparison to using standard confocal microscopy. Imaging results obtained from Alexa 594 immunolabeled tubulin (green color) and Star 635P immune-labeled vimentin (red color) samples. (Inset, top right) Results of the tubulins in the region highlighted by the dashed white box. On the lower right of each figure are results of vimentins of the same region. Inset scale bars represent 1 μm.

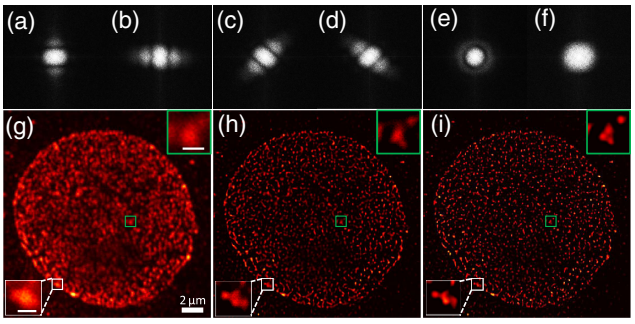

FIG. 4. Experimental examination of the SLE-based multiview NFOMM. (a–f) Fourier spectra of the recordings of nuclear pore complexes in Vero cells immune labeled by Star 635P with 0°, 90°, 135°, and 45° direction SLE, SDE, and GE. (g) Confocal microscopy result corresponding to (f). (h) NFOMM result using the BGD algorithm and the corresponding recordings for (e),(f). (i) NFOMM result using the BGD algorithm and recordings corresponding to (a–d),(f). Inset scale bars in (g) are 500 nm.

large fluorescence intensity induces detector saturation, especially for cases when imaging dense tissue regions, thereby restricting the illumination power and limiting further improvement of the resolution. To avoid this issue experimentally, a tunable attenuator was positioned before the detector to lower the intensity of the emitted fluorescence signal. In addition, we implement a narrowed pinhole scheme with diameter (0.37 A.U.) half of that used in the former experiments to further limit detection saturation. According to the confocal principle [53], a narrower pinhole not only helps with rejecting the out-of-plane fluorescence signal arriving at the detector, but also directly improves the resolution. We apply NFOMM along with this scheme, observing an improvement of transverse resolution up to ~60 nm (less than $\lambda/10$) at an illumination power of 2.1 mW [Figs. 2(d)–2(f)]. Additional details are shown in the Supplemental Material, Fig. S6 [38].

Biological imaging of SDE-based dual-view NFOMM.—Next, experiments using dual-color Vero cells are performed with dual-view NFOMM. Imaging results demonstrate that subdiffraction resolution in both transverse directions is achievable in biological samples, as evidenced by the observed fine structures of both tubulin microtubules (Alexa594 colored) and vimentin (Star635P colored) in the later NFOMM images shown in Fig. 3. These results confirm the superresolving capacity of NFOMM in multicolor biological imaging (see more details about the dual-color imaging figures in the Supplemental Material, Figs. S7 and S8 [38]). Moreover, in the Supplemental Material [Figs. S9, S10(b), and S10(c) [38]], experimental results highlight the importance of compensating for the missing spatial-frequency regions for bioimaging applications.

SLE-NFOMM with blind multiview reconstruction.—Next, as proof of concept, we experimentally demonstrate the superresolving ability using the SLE modulation. As can be seen from the optical transfer function images obtained from the corresponding recordings for different SLE orientations at the saturation illumination power [Figs. 4(a)–4(d)], the saturation effect, along with phase modulation, successfully increases the spatial-frequency extent beyond that of the GE [Fig. 4(f)] as well as the SDE [Fig. 4(e)]. Since the model-based multiview reconstruction cannot be easily applied to the SLE recordings due to aberrations, we specifically implement a blind gradient descent (BGD)-based multiview reconstruction algorithm here (see details about the BGD algorithm in the Supplemental Material, Sec. III [38]). When comparing Figs. 4(h) and 4(i) with Fig. 4(g), we observe a significant increase in resolution with the NFOMM result. Highlighted in the white and green boxes in Figs. 4(g)–4(i), the regions that once blurred in the confocal image are well discerned in the accompanied SDE-NFOMM [Fig. 4(h)] and SLE-NFOMM [Fig. 4(i)] results. Furthermore, the resolution enhancement obtained from SLE-NFOMM is clearly superior to that of SDE-NFOMM [see the green boxes in Figs. 4(h) and 4(i)], as expected from the reasoning explained above.

Discussion.—In this first demonstration, NFOMM has achieved a resolution exceeding that of SIM, ISM [54], and SAX [55]. To validate NFOMM's performance, we have compared the imaging results with the pulsed-wave STED method using the same sample (Supplemental Material, Fig. S10 [38]). NFOMM results have achieved a comparable resolution to STED. Notably, in continuous-wave STED [56], the FWHM of 60 nm was obtained using a depletion power of 160 mW according to the square root law [57], while in NFOMM, we achieve a similar resolution with a power of only 2.1 mW (Fig. 2). The much lower power requirement can be attributed partially to a larger fluorescence excitation absorption cross section in NFOMM compared to the depletion absorption cross section in STED [56]. In the experiments, NFOMM may

risk reducing the sectioning ability due to the saturation effect, which can be eliminated by shearing the Fourier spectra of the lower-frequency regions of GE recordings and the higher-frequency regions of the modulated recordings (see Supplemental Material, Sec. IV [38]).

To further demonstrate NFOMM's applicability, we apply it for imaging 3D biological structures of the Vero tubulin networks (Supplemental Material, Fig. S11, Video 1 [38]) and Vero nuclear pore complexes (Supplemental Material, Video 2 [38]) using SDE-based dual-view modulation. NFOMM achieves both high contrast and high transverse superresolution owing to the frequency shifting and the deconvolution procedures. Moreover, the 3D superresolution capacity of NFOMM is verified from preliminarily simulations (Supplemental Material, Sec. V [38]). In addition, we find that NFOMM is compatible with point-scanning-based methods such as ISM or Rescan [58], which may also help mitigate the frequency deficiency issues (see simulations in the Supplemental Material, Fig. S12 [38]).

Owing to the use of a single laser source and by exploiting excitation saturation, NFOMM obviates the deexcitation issues or incomplete depletion that occurs with STED, as well as the demand for photoswitchable dyes in single molecule localization microscopy, and thus can be simply adapted to existing confocal systems with more possible applications. Thus, NFOMM can enable superresolution 3D multicolor living cell imaging or imaging saturable inorganic media (e.g., graphene, perovskite, and even gold scattering [59], which have long, undepletable, or complex emission spectra) beyond the diffraction limit. Moreover, by having less constraints on the illumination quality and the coalignment from two beams, NFOMM is straightforward to be implemented in commercial two-photon microscopes for observing deep-tissue imaging.

A potential drawback of NFOMM is the intensified photobleaching and nonefficient saturation induced by accumulating a large number of photons in the triplet state under the excitation saturated situation [60,61]. Potential approaches to alleviate this problem include decreasing the concentration of free oxygen to minimize destructive chemical reactions and introducing the nanosecond pulsed laser with low repetition rates to allow the triplet state relaxation between the two successive pulses [62,63]. Moreover, by being flexible on the dyes used, many brighter probes, such as the quantum dots [18], can be employed, thereby enabling long-term observation. In addition, as we show in this Letter, photobleaching is not destructive in NFOMM. In the Supplemental Material, Fig. S13 [38], we give recordings on vimentins as a reference, where the amount of photobleaching per recording with a pixel dwell time of 0.1 ms and pixel per size of 15 nm is 2.5%–5%.

Aside from the conventional Gaussian illumination, the demonstrated patterns in this Letter have phase singularities and all have optical angular momentum (OAM) [64,65] in common, pointing out potential investigations for further optimizing the illumination patterns, such as increasing the OAM radial indices [66]. The NFOMM concept aims at maximizing the system frequency shifting ability using multiple phase modulations and nonlinear photon response. For future work, we anticipate incorporating phase retrieval algorithms to both help the system retrieve the PSFs [67] and optimize the illumination patterns for specific usages [68].

In summary, we have developed NFOMM as a computational superresolved imaging method able to achieve $\lambda/10$ resolution while delivering an ultimate resolution in principle. Aside from the issue of being a little more vulnerable to photobleaching, NFOMM inherits nearly all the advantages of a confocal microscope. Given its simplicity, low illumination power, and promise to be easily added onto existing confocal microscopes, we envision that NFOMM will be quickly adapted to greatly facilitate biological or material observations for fundamental studies in the future.

G. Z. appreciates Dr. Rainer Heintzmann (Friedrich-Schiller-Universität Jena) for his discussion about SIM-like postprocessing algorithms with data obtained by pointwise scanning and Dr. Jan Keller-Findeisen (Max Plank Institute For Biophysical Chemistry) for his discussion about requirements of fluorescent dyes in STED and SSIM. The authors thank Abberior Instruments for preparing the samples and the STED experiments. This work was financially sponsored by the Natural Science Foundation of Zhejiang Province LR16F050001, the National Basic Research Program of China (973 Program) (2015CB352003 Grant), the National Natural Science Foundation of China (Grants No. 61735017, No. 61427818, and No. 61335003), the Fundamental Research Funds for the Central Universities (Grant No. 2017FZA5004), and the U.S. National Institute of Health (NIH) Grant No. NIH9P41EB015871-26A1.

*G. Z. and C. Z. contributed equally to this work.
†Corresponding author.
cfkuang@zju.edu.cn
‡Corresponding author.
liuxu@zju.edu.cn

[1] S. W. Hell, Nat. Methods **6**, 24 (2009).
[2] R. Heintzmann and M. G. Gustafsson, Nat. Photonics **3**, 362 (2009).
[3] S. W. Hell and J. Wichmann, Opt. Lett. **19**, 780 (1994).
[4] R. Heintzmann and C. G. Cremer, *Proceedings of SPIE 3568, Optical Biopsies and Microscopic Techniques III* (1999), https://doi.org/10.1117/12.336833.
[5] K. Fujita, M. Kobayashi, S. Kawano, M. Yamanaka, and S. Kawata, Phys. Rev. Lett. **99**, 228105 (2007).
[6] P. J. Walla, N. Hafi, M. Grunwald, L. V. D. Heuvel, A. Timo, M. Zagrebelsky, M. Korte, and A. Munk, Nat. Methods **11**, 579 (2014).
[7] G. Zhao, M. M. Kabir, K. C. Toussaint, Jr., C. Kuang, C. Zheng, Z. Yu, and X. Liu, Optica **4**, 633 (2017).

[8] M. G. Gustafsson, J. Microsc. **198**, 82 (2000).
[9] R. Heintzmann and T. Huser, Chem. Rev. **117**, 13890 (2017).
[10] M. Petráň, M. Hadravský, M. D. Egger, and R. Galambos, J. Opt. Soc. Am. **58**, 661 (1968).
[11] M. G. Gustafsson, Proc. Natl. Acad. Sci. U.S.A. **102**, 13081 (2005).
[12] R. Heintzmann, T. M. Jovin, and C. Cremer, J. Opt. Soc. Am. A **19**, 1599 (2002).
[13] N. T. Urban, K. I. Willig, S. W. Hell, and U. V. Nägerl, Biophys. J. **101**, 1277 (2011).
[14] H. Blom and J. Widengren, Chem. Rev. **117**, 7377 (2017).
[15] P. Gao, B. Prunsche, L. Zhou, K. Nienhaus, and G. U. Nienhaus, Nat. Photonics **11**, 163 (2017).
[16] F. Bottanelli *et al.*, Nat. Commun. **7**, 10778 (2016).
[17] F. R. Winter, M. Loidolt, V. Westphal, A. N. Butkevich, C. Gregor, S. J. Sahl, and S. W. Hell, Sci. Rep. **7**, 46492 (2017).
[18] J. Hanne, H. J. Falk, F. Görlitz, P. Hoyer, J. Engelhardt, S. J. Sahl, and S. W. Hell, Nat. Commun. **6**, 7127 (2015).
[19] C. J. R. Sheppard, Optik (Stuttgart) **80**, 53 (1988).
[20] C. B. Müller and J. Enderlein, Phys. Rev. Lett. **104**, 198101 (2010).
[21] C. J. Sheppard, S. B. Mehta, and R. Heintzmann, Opt. Lett. **38**, 2889 (2013).
[22] R. W. Lu, B. Q. Wang, Q. X. Zhang, and X. C. Yao, Biomed. Opt. Express **4**, 1673 (2013).
[23] C. Kuang, Y. Ma, R. Zhou, G. Zheng, Y. Fang, Y. Xu, X. Liu, and P. T. C. So, Phys. Rev. Lett. **117**, 028102 (2016).
[24] G. P. J. Laporte, N. Stasio, C. J. R. Sheppard, and D. Psaltis, Optica **1**, 455 (2014).
[25] V. Kalosha and I. Golub, Opt. Lett. **32**, 3540 (2007).
[26] B. K. Singh, H. Nagar, Y. Roichman, and A. Arie, Light Sci. Appl. **6**, e17050 (2017).
[27] H. Lin, B. Jia, and M. Gu, Opt. Lett. **36**, 2471 (2011).
[28] C. B. Müller and J. Enderlein, Phys. Rev. Lett. **104**, 198101 (2010).
[29] J.-H. Park, C. Park, H. S. Yu, J. Park, S. Han, J. Shin, S. H. Ko, K. T. Nam, Y.-H. Cho, and Y. K. Park, Nat. Photonics **7**, 454 (2013).
[30] Y. Choi, T. D. Yang, C. Fang-Yen, P. Kang, K. J. Lee, R. R. Dasari, M. S. Feld, and W. Choi, Phys. Rev. Lett. **107**, 023902 (2011).
[31] E. G. Van Putten, D. Akbulut, J. Bertolotti, W. L. Vos, A. Lagendijk, and A. P. Mosk, Phys. Rev. Lett. **106**, 193905 (2011).
[32] B. Yang, J.-B. Trebbia, R. Baby, P. Tamarat, and B. Lounis, Nat. Photonics **9**, 658 (2015).
[33] E. Rittweger, D. Wildanger, and S. Hell, Europhys. Lett. **86**, 14001 (2009).
[34] P. P. Mondal and A. Diaspro, *Electric Field Effects in Optical Microscopy Systems* (Springer, Netherlands, 2014).
[35] M. Born and E. Wolf, Math. Gaz. **1**, 986 (1980).
[36] M. Yamanaka, Y. K. Tzeng, S. Kawano, N. I. Smith, S. Kawata, H. C. Chang, and K. Fujita, Biomed. Opt. Express **2**, 1946 (2011).
[37] C. Eggeling, A. Volkmer, and C. A. Seidel, ChemPhysChem **6**, 791 (2005).
[38] See Supplemental Material at http://link.aps.org/supplemental/10.1103/PhysRevLett.120.193901 for experimental details, a detailed demonstration of the reconstruction process, and simulations and supplementary figures of experiments, which includes Refs. [40–53].
[39] Y. Wang, J. Schnitzbauer, Z. Hu, X. Li, Y. Cheng, Z. L. Huang, and B. Huang, Opt. Express **22**, 15982 (2014).
[40] J. W. Goodman, *Introduction to Fourier Optics*, (Roberts and Company Publishers, Englewood, 2005).
[41] M. B. Cannell, A. Mcmorland, and C. Soeller, *Image Enhancement by Deconvolution* (Springer, New York, 2006).
[42] J. H. Resau, *Handbook of Biological Confocal Microscopy* (Plenum, New York, 1995).
[43] N. Chakrova, B. Rieger, and S. Stallinga, J. Opt. Soc. Am. A **33**, B12 (2016).
[44] U. Krzic, PhD thesis, Univ. Heidelberg, 2009.
[45] M. Bertero, P. Boccacci, G. Desiderà, and G. Vicidomini, Inverse Probl., **25**, 123006 (2009).
[46] S. Preibisch, F. Amat, E. Stamataki, and M. Sarov, Nat. Methods **11**, 645 (2014).
[47] D. A. Fish, A. M. Brinicombe, E. R. Pike, and J. G. Walker, J. Opt. Soc. Am. A **12**, 58 (1995).
[48] S. Dong, P. Nanda, R. Shiradkar, K. Guo, and G. Zheng, Opt. Express **22**, 20856 (2014).
[49] R. Ayuk *et al.*, Opt. Lett. **38**, 4723 (2013).
[50] N. Chakrova, R. Heintzmann, B. Rieger, and S. Stallinga, Opt. Express **23**, 31367 (2015).
[51] J. R. Swedlow, J. W. Sedat, and D. A. Agard, *Deconvolution in Optical Microscopy* (Academic Press, New York, 1996).
[52] R. Heintzmann, Micron **38**, 136 (2007).
[53] R. H. Webb, Rep. Prog. Phys. **59**, 427 (1996).
[54] O. Schulz, C. Pieper, M. Clever, J. Pfaff, A. Ruhlandt, R. H. Kehlenbach, F. S. Wouters, J. Grosshans, G. Bunt, and J. Enderlein, Proc. Natl. Acad. Sci. U.S.A. **110**, 21000 (2013).
[55] M. Yamanaka, Y.-K. Tzeng, S. Kawano, N. I. Smith, S. Kawata, H.-C. Chang, and K. Fujita, Biomed. Opt. Express **2**, 1946 (2011).
[56] K. I. Willig, B. Harke, R. Medda, and S. W. Hell, Nat. Methods **4**, 915 (2007).
[57] V. Westphal and S. W. Hell, Phys. Rev. Lett. **94**, 143903 (2005).
[58] G. M. R. De Luca, R. M. P. Breedijk, R. A. J. Brandt, C. H. C. Zeelenberg, B. E. de Jong, W. Timmermans, L. N. Azar, R. A. Hoebe, S. Stallinga, and E. M. M. Manders, Biomed. Opt. Express **4**, 2644 (2013).
[59] S.-W. Chu *et al.*, Phys. Rev. Lett. **112**, 017402 (2014).
[60] C. Ringemann, A. Schönle, A. Giske, C. von Middendorff, S. W. Hell, and C. Eggeling, ChemPhysChem **9**, 612 (2008).
[61] C. Eggeling, A. Volkmer, and C. A. Seidel, ChemPhysChem **6**, 791 (2005).
[62] M. G. Gustafsson, Proc. Natl. Acad. Sci. U.S.A. **102**, 13081 (2005).
[63] G. Donnert, C. Eggeling, and S. W. Hell, Nat. Methods **4**, 81 (2007).
[64] L. Allen, M. W. Beijersbergen, R. J. C. Spreeuw, and J. P. Woerdman, Phys. Rev. A **45**, 8185 (1992).
[65] S. Lloyd, M. Babiker, G. Thirunavukkarasu, and J. Yuan, Rev. Mod. Phys. **89**, 035004 (2017).
[66] K. Y. Bliokh, P. Schattschneider, J. Verbeeck, and F. Nori, Phys. Rev. X **2**, 041011 (2012).
[67] P. N. Petrov, Y. Shechtman, and W. Moerner, Opt. Express **25**, 7945 (2017).
[68] Y. Shechtman, S. J. Sahl, A. S. Backer, and W. E. Moerner, Phys. Rev. Lett. **113**, 133902 (2014).